Disordered Elastic Metasurfaces

Liyun Cao,[1,2] Zhichun Yang,[1,†] Yanlong Xu,[1] Shi-Wang Fan,[2] Yifan Zhu,[2] Zhaolin Chen,[1] Brice Vincent,[2] and Badreddine Assouar[2,*]

[1] *School of Aeronautics, Northwestern Polytechnical University, Xi'an, 710072, China*
[2] *Institut Jean Lamour, CNRS, Université de Lorraine, Nancy, 54506, France*

(Received 25 July 2019; revised manuscript received 22 October 2019; published 28 January 2020)

The discovery of the disorder effect in traditional metamaterials has opened up possibilities in the search for disordered metasurfaces. Photonic, dielectric, and elastic metamaterials that exhibit added value of the disorder effect on wave-propagation physics are reported. Despite this extensive attention and progress in disordered metamaterials, elastic metasurfaces, however, involving disorder have not yet been reported. Here, we introduce the concept of disordered elastic metasurface composed of identical pillared resonators with a random arrangement in the subwavelength range. Based on theoretical formalism and direct acoustic measurement, we observe anomalous deflection and focusing effects of flexural waves in a plate and elucidate, in detail, the related physics. This research extends the disorder effect to metasurfaces and may lead to innovative acoustoelastic devices.

DOI: 10.1103/PhysRevApplied.13.014054

I. INTRODUCTION

Since the emergence of metamaterials, the study of disorder has become an important research direction [1–3]. A deep understanding of the disorder effect can help to improve the properties of metamaterials [4,5] and enrich their physics [6–9]. For instance, disorder can widen the band gap in elastic metamaterials [5] and induce topological-state transition in photonic metamaterials [8] or phase transitions in dielectric metamaterials [9]. In contrast, independent of the spatial organization of the material, the invariant band gaps of metamaterials can also be observed by taking advantage of strong localization effects [10]. As a consequence, a detailed analysis of wave properties in disordered metamaterials is of interest, not only for physics, but also for pragmatic applications. Recently, as one ultrathin kind of metamaterials [11–13], optic metasurfaces [14,15] and acoustic metasurfaces [16–19] have been proposed to realize extraordinary wave manipulation. For elastic waves, due to complex wave coupling, the elastic metasurface design [20,21] is of paramount significance to current research efforts in a large variety of applications, ranging from ultrasonic detection to vibration control. Recently, disorder was introduced into the optic metasurface [22], which exhibited additional unique features for wave-front shaping, such as a tailorable angular-scattering profile. However, acoustic or elastic metasurfaces involving disorder have not yet been reported.

Here, we introduce the concept of disordered elastic metasurface (DEM) composed of identical pillared resonators, with a random arrangement in the subwavelength range. We analytically and numerically reveal the decoupled region of the pillared resonators. The phase shifts and transmission amplitudes of the subunits are only linearly related to the number of resonators and independent of the spatial arrangement of resonators. The disorder releases the degree of freedom of pillar position in the subunit, which can greatly enhance the flexibility for the reconfigurable subunit. Both numerical simulations and experiments are carried out to demonstrate the extraordinary functionalities of the DEM, including anomalous deflection and focusing. The physics of disorder in the proposed metasurface can be regarded as a universal method for transmissive metasurfaces and metastructure designs. The DEM may also have a direct pragmatic variety of applications in the field of controllable wave manipulation and related acoustoelastic devices and wave engineering.

II. MODEL AND DESIGN

Figure 1(a) shows a schematic of the DEM with predesigned geometries comprising an array of subunits that is capable of manipulating a flexural wave in a plate. The 3D subunit is constructed based on pillared resonators in Fig. 1(b). The corresponding two-dimensional (2D) model of the subunit is depicted in Fig. 1(c). All attached resonators have the same geometrical parameters: thickness

*badreddine.assouar@univ-lorraine.fr
†yangzc@nwpu.edu.cn

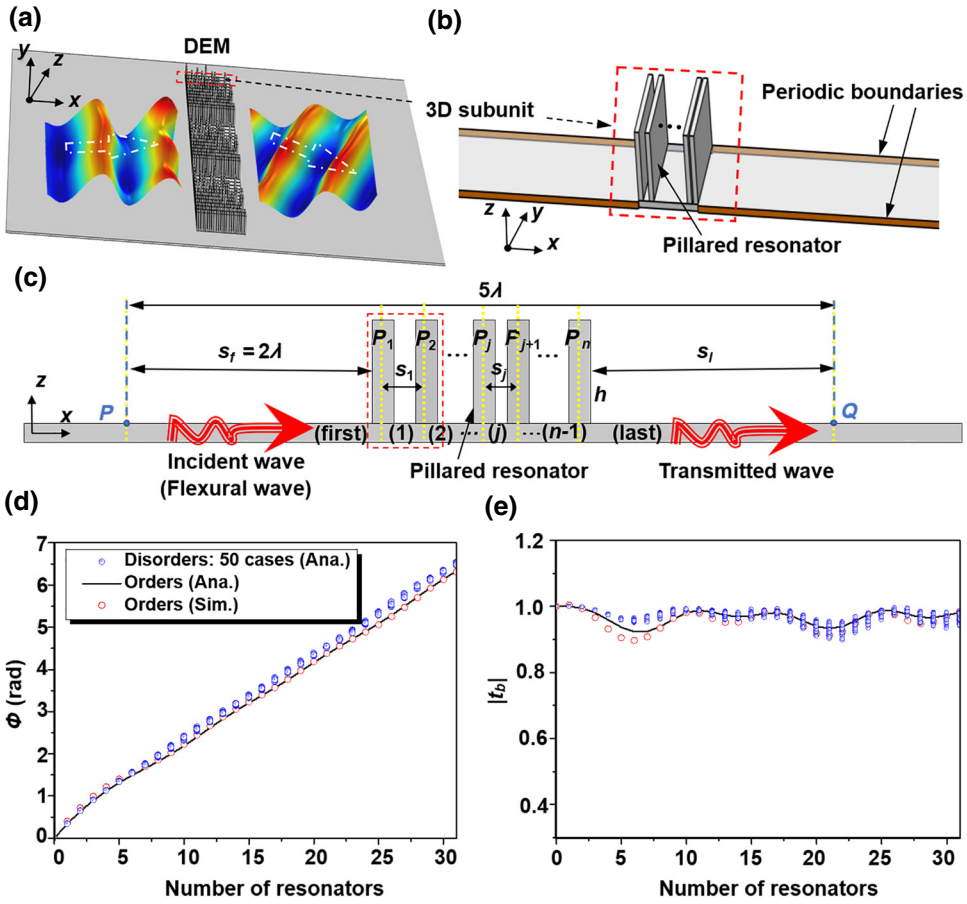

FIG. 1. Disordered elastic metasurface. (a) Schematic diagram of DEM. (b) Three-dimensional (3D) view of a subunit. (c) Cross-section view of a subunit. The phase shift (d) and transmission amplitude (e) solved analytically and numerically for disordered and ordered resonators as function of the number of resonators in the subwavelength subunit.

d_2 and height h are 3 and 30 mm, respectively. The resonators are attached to the plate with a disordered arrangement, i.e., the spacing, s_j, between the jth resonator and $(j+1)$th resonator is arbitrary. Considering both flexural and longitudinal waves propagate in the hosting plate and resonators, the coefficient vectors of the wave fields at point P of the incident region and point Q of the transmitted region [marked in Fig. 1(c)] are denoted as $\mathbf{k}_{\text{in}} = [1, r_b,\ 0,\ r_b^*,\ 0,\ r_l]^T$ and $\mathbf{k}_{\text{out}} = [t_b,\ 0,\ t_b^*,\ 0,\ t_l,\ 0]^T$ (see details in Appendix A), respectively. $r_b, t_b, r_b^*, t_b^*, r_l$, and t_l are the amplitude ratios of the reflected propagating flexural wave, transmitted propagating flexural wave, reflected evanescent flexural wave, transmitted evanescent flexural wave, reflected propagating longitudinal wave, and transmitted propagating longitudinal wave to the incident propagating flexural wave, respectively.

The transfer equation for the disordered multiresonator shown in Fig. 1(c) (the detailed derivation can be found in Appendix A) is

$$\mathbf{k}_{\text{out}} = N_2^{(\text{last})} N_1 N_2^{(n-1)} N_1 \cdots N_2^{(2)} N_1 N_2^{(1)} N_1 N_2^{(\text{first})} \mathbf{k}_{\text{in}}, \quad (1)$$

where n is the number of the pillared resonator, N_1 is the transfer matrix for the incident wave propagating from left to right of the pillared resonator. $N_2^{(1)}, N_2^{(2)}, \ldots$, and $N_2^{(n-1)}$ are the transfer matrices for the flexural and longitudinal waves propagating in the plate regions with pillar spacing $s_1, s_2, \ldots$, and s_{n-1}, respectively. $N_2^{(\text{first})}$ and $N_2^{(\text{last})}$ are the transfer matrices for waves propagating in the first and last regions, respectively. For the subunit with a different number of resonators, we randomly adjust the pillar spacing, s_j, between the jth resonator and $(j+1)$th resonator, which meets the relation of $nd_2 < \sum_{j=1}^{n-1} s_j < \lambda$, to ensure that the total multiresonator thickness does not exceed one wavelength λ, i.e., subwavelength thickness. In this way, for a different number of attached resonators, 50 disordered subunits are randomly built without loss of generality. To calculate the phase shift and transmission amplitude analytically, we assume that the pillared resonators and plate are made of aluminum alloy. The excitation frequency is selected as 1 kHz and the corresponding flexural-wave wavelength for the plate with a thickness of 3 mm is 57.1 times the pillar thickness ($d_2 = 3$ mm). The transmission amplitude, $|t_b|$, at point Q is calculated analytically from Eq. (1), and the corresponding phase shift is extracted from the complex transmission coefficient t_b (see details in Appendix A).

In Figures 1(d) and 1(e), the analytical results of the phase shift and transmission amplitude of the flexural waves across the disordered subunits are plotted as blue

circles. Several interesting phenomena can be observed as follows. First, randomly disrupting the arrangement of resonators has almost no effect on the phase shift and transmission amplitude. In other words, the phase shift and transmission amplitude are only related to the number of resonators in the subunits, but independent of the arrangement. This indicates that the designed metasurface has a stronger robustness than that of conventional designs. Second, the phase shifts by varying the number of resonators can span over a full phase range of 2π with high transmission amplitude (bigger than 0.9). This ensures the high efficiency of the metasurface for fine field manipulations [23,24]. Third, the phase shift increases linearly with the number of resonators. This allows us to simply predict the phase shift of these subunits with a different number of resonators.

Furthermore, the ordered arrangements of resonators are also investigated for comparison, with all pillar spacings fixed uniformly at 5 mm without loss of generality. The transmission coefficient, t_b, can be calculated analytically from the modified transfer equation, $\mathbf{k}_{\text{out}} = N_2^{(\text{last})} N_1 (N_2^* N_1)^{n-1} N_2^{(first)} \mathbf{k}_{\text{in}}$ (see details in Appendix A), where N_2^* is the transfer matrix for the wave propagating in the plate region of the identical pillar spacings. The phase shift and transmission amplitude, by varying the number of resonators, are solved analytically and numerically (plotted as black solid lines and red circles) in Figs. 1(d) and 1(e). The simulated results are in good agreement with those obtained analytically, which confirms the accuracy of the analytical method. Meanwhile, the results for the ordered resonators are very close to the disordered ones, showing that the introduction of disorder does not affect the phase shift and transmission amplitude.

III. THE PHYSICS OF DECOUPLED DISORDERED SUBUNITS

To explain these phenomena, we investigate the model for two adjacent resonators in the subunit, as marked with the red dotted box in Fig. 1(c). Specifically, we analyze the influence of the excitation frequency, f; the typical structural parameter, h (pillar height); and the pillar spacing, s_1, on the phase, ϕ_1, and transmission amplitude, $|t_1|$, of point Q in Fig. 1(c). The remaining parameters are the same as those discussed above. The phase, ϕ_1, and transmission amplitude, $|t_1|$, can be expressed as $\phi_1 = G_{\phi 1}(f,h,s_1)$ and $|t_1| = G_{|t1|}(f,h,s_1)$, respectively. From the above analysis of the disorder unit, it can be seen that, under certain conditions, the phase and transmission amplitude are independent of the pillar spacing. For a quantitative evaluation of the dependence of phase and transmission amplitude on the pillar spacing, we define the coupling strengths as

$$\Lambda_{\phi_1,s_1}(f,h,s_1) = \frac{\partial G_{\phi_1}(f,h,s_1)}{\partial s_1}, \tag{2}$$

$$\Lambda_{|t_1|,s_1}(f,h,s_1) = \frac{\partial G_{|t_1|}(f,h,s_1)}{\partial s_1}. \tag{3}$$

We further obtain the coupling coefficients $\bar{\Lambda}_{\phi_1,s_1}(f,h)$ and $\bar{\Lambda}_{|t_1|,s_1}(f,h)$ by integrating the coupling strengths for all different pillar spacings (0.003λ, λ) and conducting normalization with respect to their maxima. The effects of changing f and h on the coupling coefficients $\bar{\Lambda}_{\phi_1,s_1}$ and $\bar{\Lambda}_{|t_1|,s_1}$ are shown analytically in Figs. 2(a) and 2(b), respectively. These results clearly show the existence of completely decoupled regions characterized by $\bar{\Lambda}_{\phi_1,s_1} = 0$

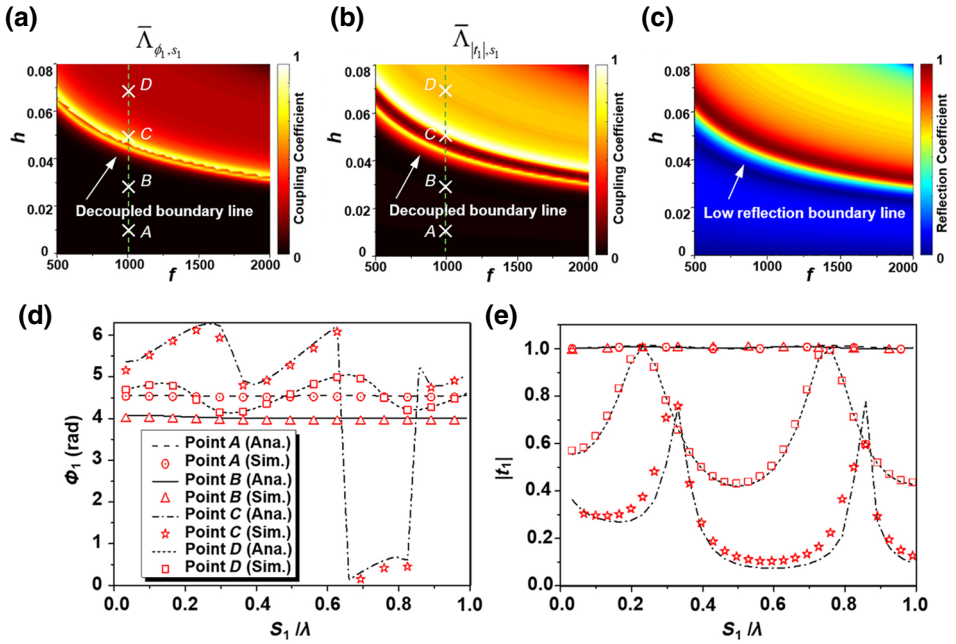

FIG. 2. The physics of decoupled disordered resonators. (a),(b) Effect of changes of f and h on the analytical coupling coefficients $\bar{\Lambda}_{\phi_1,s_1}$ and $\bar{\Lambda}_{|t_1|,s_1}$, respectively. (c) Analytical reflection coefficient for a single resonator by varying the excitation frequency, f, and resonator height, h. For points A, B, C, and D in (a) and (b), the phase and transmission amplitude in the far field (point Q) by varying the pillar spacings are analytically and numerically shown in (d) and (e), respectively.

and $\bar{\Lambda}_{|t_1|,s_1} = 0$, respectively, which means that the phase shift and transmission amplitude are independent of the pillar spacing. The marked decoupled boundary lines of the phase and transmission amplitude are almost at the same location.

To further reveal the underlying physics, the reflection coefficient of a single resonator, by varying the excitation frequency, f, and resonator height, h, is analytically obtained (see details in Appendix A), as shown in Fig. 2(c). We label the low-reflection boundary line and observe that the decoupled boundary lines for the phase and transmission amplitude are consistent with the low-reflection boundary line. This indicates that the decoupling of the phase and transmission amplitude, with respect to the pillar spacing, depends on the low reflection intensity of the incident wave passing through the resonator. Therefore, the low reflection coupling between resonators induced from their low reflection intensity will lead to decoupling, which releases the degree of freedom of the pillar position in the subunit. It should be pointed out that the Fabry–Perot resonance, where the phases equal an integer multiple of π, also has a low reflection intensity. However, it does not lead to the above decoupling. The proposed physics can broaden an understanding of metamaterials and be applied to other transmissive metasurfaces for optics, acoustics, and elastics.

For intuitively displaying the above analysis conclusions, predictive decoupled points A and B and coupling points C and D are chosen from Figs. 2(a) and 2(b). For these four points, the phase and transmission amplitude in the far field, as a function of the pillar spacing, are solved analytically and numerically. The results are shown in Figs. 2(d) and 2(e). One can observe that the phase and transmission amplitude at points A and B are independent of the pillar spacing, while, at points C and D, they are strongly dependent on pillar spacing. These results confirm the validity of our theoretical prediction. Point B in the decoupled region corresponds to the above disordered subunit analyzed in Figs. 1(d) and 1(e).

IV. DEM MANIPULATING THE FLEXURAL WAVE

The above-designed 2D disordered subunits can be extended directly to the corresponding 3D ones with slots (see in Appendix B), while the phase shift and transmission amplitude remain almost unchanged. The elastic metasurfaces are designed by the 3D disordered subunits. Different numbers of pillared resonators are attached on the hosting plate with slots (see Appendix C) to achieve different functions, including anomalous deflection and focusing. Importantly, these resonators can be conveniently disassembled and reattached, since the disordered and ordered resonators have the same effect on wave manipulation. It is convenient to continuously change the phase shift for every subunit by changing their number of resonators. It should be noted that the reconfigurable subunit can be

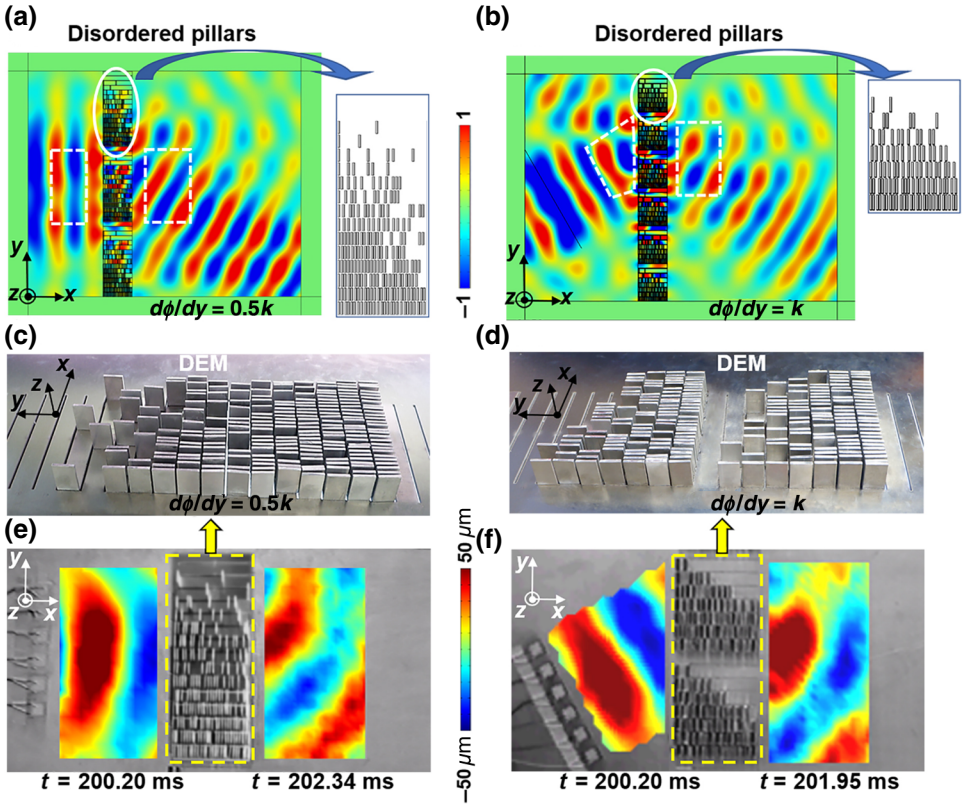

FIG. 3. Deflecting flexural wave with DEM. (a),(b) Wave fields for vertically and obliquely incident Gaussian beams passing through two disordered metasurfaces with phase shift gradients of $d\phi/dy = 0.5k$ and $d\phi/dy = k$, respectively. (c),(d) Fabricated metasurfaces. (e),(f) Full-field experimental measurements, including the incident and transmitted fields at different time points. The incident and transmitted fields of (e) are measured at 200.20 and 202.34 ms, respectively.

designed (a detailed design can be found in Appendix D) based on the disordered subunit. Disorder can greatly enhance flexibility for the reconfigurable subunit because it releases the degree of freedom of the pillar position in the subunit.

A. Simulations and experiments of the anomalous deflections

The DEM with the functions of anomalous deflection is designed. The corresponding individual supercells are shown in the right of Figs. 3(a) and 3(b). They are composed of eight types of chosen disordered 3D subunits, composed of 0, 2, 6, 11, 15, 19, 23, and 27 identical pillared resonators in a random arrangement. These subunits can make transmitted waves with phase shifts covering the full range of 2π and high transmittance, according to Figs. 1(d) and 1(e). The discrete phase shift of the transmitted wave increases linearly along the y axis, and the spatial phase-shift gradients for Figs. 3(a) and 3(b) are $d\phi/dy = 0.5k$ and $d\phi/dy = k$, respectively, where $k = 2\pi/\lambda$. According to the generalized Snell law [14], for the vertically and obliquely (an incident angle of 30°) incident waves, the theoretical refraction angles are 30° and −30°, respectively. Full-wave simulations (detailed geometric parameters of the units and more associated simulation details are provided in Appendixes C and E) clearly demonstrate the anomalous deflections. The ordered elastic metasurface is also constructed for comparison, as shown in Appendix F. The metasurfaces with subunits possessing the required phase shifts are fabricated and shown in Figs. 3(c) and 3(d). The full-field experimental measurements, including the incident and transmitted fields at different time points, are shown in Figs. 3(e) and 3(f), which are in good agreement with both the analytical predictions and simulated results. Detailed propagation phenomena are presented in Movie S1 and Movie S2 within the Supplemental Material [25].

B. Simulation and experiment of the focusing

By employing the disordered subunits, our metasurface design can also be exploited to achieve flexural-wave focusing, as shown in Fig. 4(e). The DEM can be readily

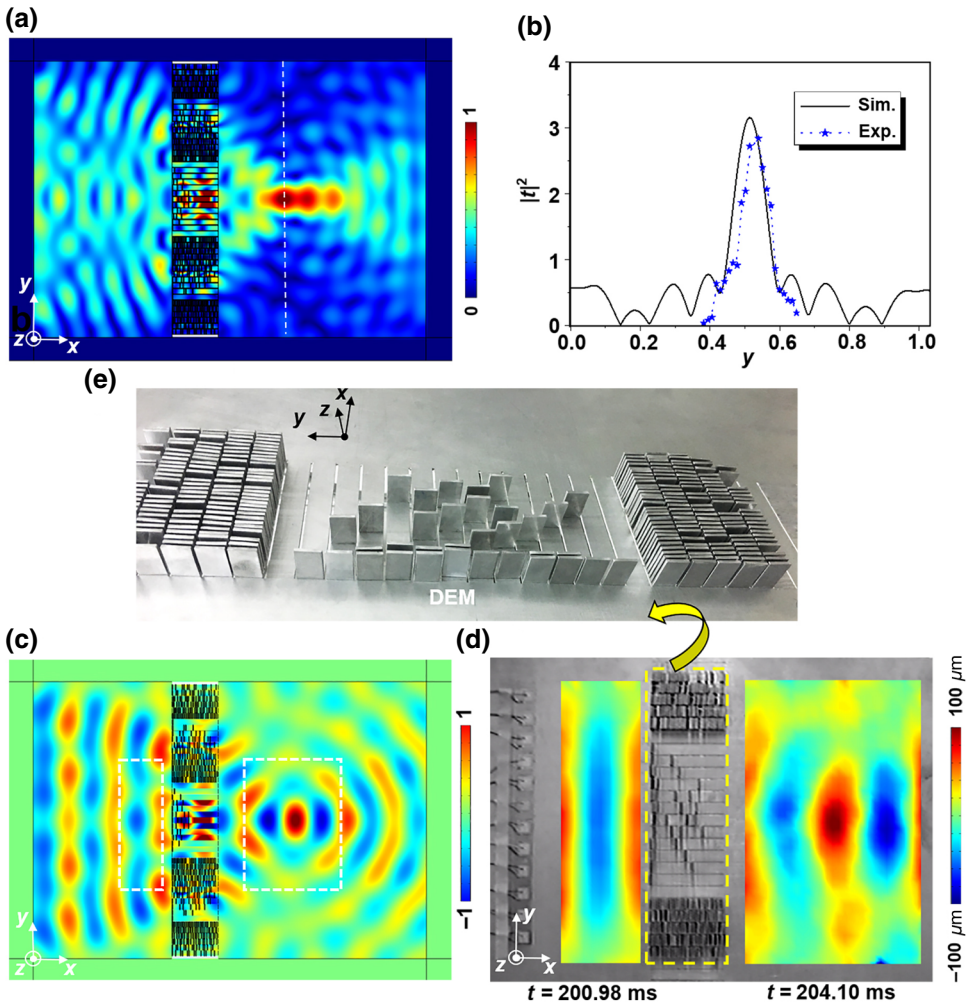

FIG. 4. Focusing flexural wave with DEM. (a),(c) Simulated results of the transmitted intensity and displacement fields, with focus at 1.5λ, for the DEM, respectively. (b) Normalized transmitted intensity fields at the focal spot along the y direction from the simulation and experiment. (e) Fabricated structure of the DEM. (d) Full-field experimental measurement.

constructed by selecting units that match the requested hyperbolic phase profile, $\phi(y) = (2\pi/\lambda)(\sqrt{F^2 + y^2} - F)$, where $F = 1.5\lambda$ is the desired focal distance (detailed geometric parameters of the DEM are provided in Appendix C). The transmitted intensity and displacement fields, with focus at 1.5λ, are simulated and shown in Figs. 4(a) and 4(c), respectively. One clearly observes a focal spot after the incident waves pass through the DEM. The full-field experimental measurement is shown in Fig. 4(d). The detailed propagation phenomenon is presented in Movie S3 within the Supplemental Material [25]. For a more quantitative comparison, the normalized intensity fields of the transmitted wave at the focal spot along the y direction from the simulations and experiments are shown in Fig. 4(b). Sharp peak values are observed, which are more than three times the intensity of the incident wave. The experimental measurement is in good agreement with the simulated result and demonstrates a fine-focusing capability.

V. CONCLUSION

We report a feature of elastic metasurfaces composed of identical pillared resonators. By reducing the reflection coupling between resonators below the low-reflection boundary line in parameter space, the dependence of resonators in the subwavelength subunits on the spatial arrangement can be adjusted from existence to absence. In the decoupled region of the disordered resonators, the transmitted waves pass through the subunits with approximately full transmission, while the phase shift can be continuously adjusted by the number of resonators in the disordered spatial arrangements. In addition, we perform full-wave experimental measurements of DEM structures to demonstrate multifunctionality, including anomalous deflection and focusing. Our findings are of significance in understanding the physics of elastic wave interactions with disordered artificial media. The present work may open up avenues for a variety of applications in the field of controllable wave manipulation and related acoustoelastic devices.

ACKNOWLEDGMENT

This work is supported by the project CARNOT ICEEL "METACOM" and la Région Grand Est, by the National Natural Science Foundation of China (Grants No. 11972296 and No. 11602194), by the 111 Project (Grant No. BP0719007), and by the Natural Science Basic Research Plan in Shaanxi Province of China (Grant No. 2018JQ1076). L.C. is grateful for the support from the Innovation Foundation for Doctor Dissertation of Northwestern Polytechnical University (Grant No. CX201936) and China Scholarship Council (CSC Grant No. 201806290176).

APPENDIX A: ANALYTICAL SOLUTION FOR DISORDERED AND ORDERED SUBUNITS

1. Analytical modeling

The host plate in the subunit can be divided into several regions, which are marked as first, 1, 2, ..., j, ..., $n-1$, and last in Fig. 1(c). The governing equations for the flexural wave and longitudinal wave in the plate can be expressed as the following forms, respectively:

$$E_1 I_1 \frac{\partial^4 w(x,t)}{\partial x^4} + \rho_1 d_1 \frac{\partial^2 w(x,t)}{\partial t^2} = 0$$
$$\frac{E_1}{(1-\nu_1{}^2)} \frac{\partial^2 u(x,t)}{\partial x^2} - \rho_1 \frac{\partial^2 u(x,t)}{\partial t^2} = 0, \qquad \text{(A1)}$$

where E_1 is the Young's modulus of the hosting plate, ρ_1 is the density of the plate, and I_1 is the moment of area of the plate. $I_1 = {d_1}^3/[12(1-\nu_1{}^2)]$, in which d_1 and ν_1 are the thickness and Poisson's ratio of the plate, respectively.

The governing equation of flexural waves in region j is a fourth-order partial derivative equation. The wave number has four solutions, i.e., two real wave numbers and two complex wave numbers. The real and complex wave numbers represent propagating flexural and evanescent flexural waves, respectively. Therefore, the general solution of displacement for the governing equation is

$$w^{(j)}(x,t) = [A^{(j)} e^{-ik_{b1}x} + B^{(j)} e^{ik_{b1}x} + C^{(j)} e^{-k_{b1}x} + D^{(j)} e^{k_{b1}x}] e^{i\omega t}, \qquad \text{(A2)}$$

where the superscript (j) indicates region j. $A^{(j)}$, $B^{(j)}$, $C^{(j)}$, and $D^{(j)}$ are complex coefficients. $A^{(j)}e^{-ik_{b1}x}$ and $B^{(j)}e^{ik_{b1}x}$ correspond to the positive and negative propagating flexural waves, respectively. $C^{(j)}e^{-k_{b1}x}$ and $D^{(j)}e^{k_{b1}x}$ correspond to the positive and negative evanescent flexural waves, respectively. The flexural wave number is $k_{b1} = (\rho_1 d_1 \omega^2 / E_1 I_1)^{1/4}$, in which $\omega = 2\pi f$ is the circular frequency. The general solution of the displacement for the second-order partial derivative governing equation of longitudinal waves in region j is

$$u^{(j)}(x,t) = [P^{(j)} e^{-ik_{l1}x} + Q^{(j)} e^{ik_{l1}x}] e^{i\omega t}, \qquad \text{(A3)}$$

where the longitudinal wave number is $k_{l1} = \{[\rho_1 \omega^2 (1-\nu_1{}^2)]/E_1\}^{1/2}$; $P^{(j)}e^{-ik_{l1}x}$ and $Q^{(j)}e^{ik_{l1}x}$ correspond to the positive and negative propagating longitudinal waves, respectively.

The governing equations for the flexural wave and the longitudinal wave in the pillared resonator is similar to that in the host plate. The general solutions of the displacements for the flexural wave and longitudinal wave

equations in the pillared resonator j are

$$\begin{aligned} w^{(P_j)}(z,t) &= [A^{(P_j)}e^{-ik_{b2}z} + B^{(P_j)}e^{ik_{b2}z} + C^{(P_j)}e^{-k_{b2}z} \\ &\quad + D^{(P_j)}e^{k_{b2}z}]e^{i\omega t}, \\ u^{(P_j)}(z,t) &= [P^{(P_j)}e^{-ik_{l2}z} + Q^{(P_j)}e^{ik_{l2}z}]e^{i\omega t} \end{aligned} \tag{A4}$$

respectively. Superscript (P_j) indicates the pillared resonator j. The flexural and longitudinal wave numbers are $k_{b2} = (\rho_2 d_2 \omega^2 / E_2 I_2)^{1/4}$ and $k_{l2} = \{[\rho_2 \omega^2 (1-\nu_2{}^2)]/E_2\}^{1/2}$, respectively. E_2, ρ_2, and I_2 are the Young's modulus, density, and area moment of inertia of the pillared resonator, respectively. $I_2 = {d_2}^3/[12(1-\nu_2{}^2)]$, in which d_2 and ν_2 are the thickness of the resonator and Poisson's ratio of the material, respectively.

The relationships between slope φ and displacement w, between shear force V and displacement w, between bending moment M and displacement w, and between axial force F and displacement u are

$$\begin{aligned} \varphi &= w' \\ V &= -EIw''' \\ M &= EIw'' \\ F &= \tfrac{Ed}{(1-\nu^2)}u', \end{aligned} \tag{A5}$$

respectively. Among the right interface of region j-1, the left interface of region j, and the lower interface of resonator j, the following boundary conditions must be satisfied:

(1) Displacement continuity in x and z directions

$$\begin{aligned} u^{(j-1)} &= u^{(j)} = -w^{(P_j)} \\ w^{(j-1)} &= w^{(j)} = u^{(P_j)} \end{aligned} \tag{A6}$$

(2) Slope continuity

$$\frac{\partial w^{(j-1)}}{\partial x} = \frac{\partial w^{(j)}}{\partial x} = \frac{\partial w^{(P_j)}}{\partial z} \tag{A7}$$

(3) Force balance in x and z directions

$$\begin{aligned} &\tfrac{E_1 d_1}{(1-\nu_1{}^2)}\tfrac{\partial u^{(j-1)}}{\partial x} - \tfrac{E_1 d_1}{(1-\nu_1{}^2)}\tfrac{\partial u^{(j)}}{\partial x} - E_2 I_2 \tfrac{\partial^3 w^{(P_j)}}{\partial z^3} = 0 \\ &-E_1 I_1 \tfrac{\partial^3 w^{(j-1)}}{\partial x^3} + E_1 I_1 \tfrac{\partial^3 w^{(j)}}{\partial x^3} - \tfrac{E_2 d_2}{(1-\nu_2{}^2)}\tfrac{\partial u^{(P_j)}}{\partial z} = 0 \end{aligned} \tag{A8}$$

(4) Moment balance

$$E_1 I_1 \frac{\partial^2 w^{(j-1)}}{\partial x^2} - E_1 I_1 \frac{\partial^2 w^{(j)}}{\partial x^2} - E_2 I_2 \frac{\partial^2 w^{(P_j)}}{\partial z^2} = 0 \tag{A9}$$

(5) Forces and moment are zero at the free boundary of resonator j

$$\begin{aligned} &-E_2 I_2 \left.\frac{\partial^3 w^{(P_j)}}{\partial z^3}\right|_{z=h} = \left.\frac{E_2 d_2}{(1-\nu_2{}^2)}\frac{\partial u^{(P_j)}}{\partial z}\right|_{z=h} \\ &= E_2 I_2 \left.\frac{\partial^2 w^{(P_j)}}{\partial z^2}\right|_{z=h} = 0 \end{aligned} \tag{A10}$$

2. The transfer equation for the disordered multiresonator

The complex coefficients $A^{(j)}$, $B^{(j)}$, $C^{(j)}$, $D^{(j)}$, $P^{(j)}$, and $Q^{(j)}$ for region j in the plate can be organized as a vector

$$\mathbf{k}^{(j)} = \{A^{(j)}, B^{(j)}, C^{(j)}, D^{(j)}, P^{(j)}, Q^{(j)}\}^T. \tag{A11}$$

Among the right interface of region $j-1$, the left interface of region j, and the lower interface of resonator j, substituting Eqs. (A2)–(A4) into the boundary conditions, i.e., Eqs. (A6)–(A10), we obtain

$$\mathbf{k}_L^{(j)} = N_1 \mathbf{k}_R^{(j-1)}, \tag{A12}$$

where $\mathbf{k}_R^{(j-1)}$ and $\mathbf{k}_L^{(j)}$ indicate the coefficient vectors in the right interface of region $j-1$ and the left interface of region j, respectively. N_1 is the transfer matrix for waves propagating from left to right of the pillared resonator j, and it includes the contribution of the pillared resonators.

The relationship between the vector $\mathbf{k}_R^{(j)}$ at the right interface of region j and the vector $\mathbf{k}_L^{(j)}$ at the left interface of region j can be expressed as follows:

$$\mathbf{k}_R^{(j)} = N_2|_{s=s_j} \mathbf{k}_L^{(j)} = N_2^{(j)} \mathbf{k}_L^{(j)}, \tag{A13}$$

where

$$N_2 = \begin{pmatrix} e^{-ik_{b1}\cdot s} & 0 & 0 & 0 & 0 & 0 \\ 0 & e^{ik_{b1}\cdot s} & 0 & 0 & 0 & 0 \\ 0 & 0 & e^{-k_{b1}\cdot s} & 0 & 0 & 0 \\ 0 & 0 & 0 & e^{k_{b1}\cdot s} & 0 & 0 \\ 0 & 0 & 0 & 0 & e^{-ik_{l1}\cdot s} & 0 \\ 0 & 0 & 0 & 0 & 0 & e^{ik_{l1}\cdot s} \end{pmatrix}$$

is the transfer matrix for waves propagating between the two ends of region j.

The exciting point is assumed as point P on the plate surface, as shown in Fig. 1(c). For the first region with length $s_f = 2\lambda$, the vector $\mathbf{k}_R^{(\text{first})}$ at the right interface and the vector $\mathbf{k}_{\text{in}}$ at the left interface of the first region can be expressed as

$$\mathbf{k}_R^{(\text{first})} = N_2|_{s=2\lambda} \cdot \mathbf{k}_{\text{in}} = N_2^{(\text{first})} \cdot \mathbf{k}_{\text{in}}. \tag{A14}$$

The examined point for the transmission phase and amplitude is fixed at point Q, as shown in Fig. 1(c). For the last region, with length s_l, the vector $\mathbf{k}_{\text{out}}$ at the right end and the vector $\mathbf{k}_L^{(\text{last})}$ at the left end can be expressed as

$$\mathbf{k}_{\text{out}} = N_2|_{s=s_l^*} \cdot \mathbf{k}_L^{(\text{last})} = N_2^{(\text{last})} \cdot \mathbf{k}_L^{(\text{last})}, \tag{A15}$$

where $s_l^* = s_l - 0.08nd_2 \approx 3\lambda - \sum_{j=1}^{n-1}(s_j + 0.08d_2)$ is the modified length of the last region.

According to Eqs. (A12)–(A15), for waves propagating from the left interface of the first region to the right interface of the last region, the transfer relationship can be expressed as

$$\mathbf{k}_{\text{out}} = N_2^{(\text{last})} N_1 N_2^{(n-1)} N_1 \cdots N_2^{(2)} N_1 N_2^{(1)} N_1 N_2^{(first)} \mathbf{k}_{\text{in}}. \tag{A16}$$

From Eq. (A16), we can solve the transmission amplitude for the flexural wave transmitting through these n resonators. To do this, we make an incident positive flexural wave of $1e^{i\omega t}$ at the left interface of the first region, so the wave fields at the left interface of the first region and the right interface of the last region can be expressed as follows:

$$\begin{aligned} w_L^{(\text{first})}(x,t) &= (1 + r_b + r_b{}^*)e^{i\omega t} \\ u_L^{(\text{first})}(x,t) &= r_l e^{i\omega t} \\ w_R^{(\text{last})}(x,t) &= (t_b + t_b^*)e^{i\omega t} \\ u_R^{(\text{last})}(x,t) &= t_l e^{i\omega t}, \end{aligned} \tag{A17}$$

where r_b, t_b, r_b^*, t_b^*, r_l, and t_l are the amplitude ratios of the reflected propagating flexural wave, the transmitted propagating flexural wave, the reflected evanescent flexural wave, the transmitted evanescent flexural wave, the reflected longitudinal wave, and the transmitted longitudinal wave to the incident positive propagating flexural wave, respectively. Therefore, the vectors $\mathbf{k}_{\text{in}}$ and $\mathbf{k}_{\text{out}}$ can be written as

$$\begin{aligned} \mathbf{k}_{\text{in}} &= [1, r_b, 0, r_b^*, 0, r_l]^T \\ \mathbf{k}_{\text{out}} &= [t_b, 0, t_b^*, 0, t_l, 0]^T. \end{aligned} \tag{A18}$$

The transfer equation for the single resonator can be expressed as

$$\mathbf{k}_{\text{out}} = N_2^{(\text{last})} N_1 N_2^{(first)} \mathbf{k}_{\text{in}}. \tag{A19}$$

3. The transfer equation for the ordered multiresonator

For the ordered subunits, all pillar spacings are fixed uniformly at $s_j = 5$ mm. The corresponding transfer matrix for a wave propagating from the left interface to the right interface of uniform region j is written as $N_2^* = N_2|_{s=0.005}$. For waves propagating from the left interface of the first region to the right interface of the last region in the ordered subunit, the transfer equation can be expressed as

$$\mathbf{k}_{\text{out}} = N_2^{(\text{last})} N_1 (N_2^* N_1)^{n-1} N_2^{(first)} \mathbf{k}_{\text{in}}. \tag{A20}$$

4. Analytical solution for transmission phase shift and amplitude

According to Eqs. (A16), (A19), and (A20), r_b, r_b^*, r_l, t_b, t_b^*, and t_l can be solved with the aid of MATLAB code. $|t_b|$ is the amplitude ratio between the transmitted propagating flexural wave and the incident propagating flexural wave. The phase can be obtained from the complex amplitude ratio, t_b. The phase shift is obtained by subtracting the phase at point Q for the plate with the resonators from that of the plate without resonators. It can be calculated by

$$\phi = \begin{cases} \pi + \arctan\left[\frac{\text{imag}(t_b)}{\text{real}(t_b)}\right] & \text{if real}(t_b) < 0 \\ \arctan\left[\frac{\text{imag}(t_b)}{\text{real}(t_b)}\right] & \text{if real}(t_b) > 0 \end{cases}. \tag{A21}$$

Eq. (A21) will make the value of the phase shift from zero to 2π.

APPENDIX B: DESIGN FROM THE 2D SUBUNIT TO THE 3D ONE

The designed subunit is embodied in its 2D model. To manipulate flexural waves, the subunit should be designed as the corresponding 3D one in Fig. 5(a), which can be formed by simply stretching the 2D model in Fig. 1(c). The stretched width is denoted as w_1. Because the metasurface is formed by periodically integrating different 3D subunits, the 3D subunit should be analyzed by applying the periodic boundary conditions on the two long boundaries in the 3D striplike model in Fig. 5(a). Therefore, the formed 3D subunit is equivalent to the corresponding 2D one in Fig. 1(c). However, slots should be cut from the 3D subunit to separate adjacent different 3D subunits in the integrated metasurface, as shown in Fig. 5(b). The aim is to avoid Fano interference [26] between the adjacent different 3D subunits to independently design the subunits.

The filling ratio of the slots in one subunit is denoted as η, which is defined as dividing the slot width by the stretched width, w_1, in a subunit. In our designs, the widths of the processed pillared resonator, w_0, and the slot are 20.4 and 1 mm, respectively, i.e., $w_1 = 21.4$ and $\eta = 0.047$. The slots are very small relative to the stretched width of the subunit. The small slot will lead to a very small flexural wave scattering, which will not affect the transmission

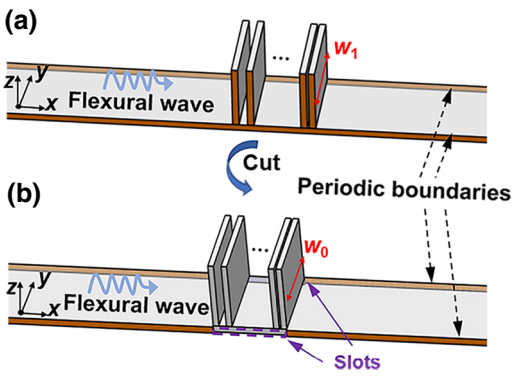

FIG. 5. (a) Model diagram of the 3D subunit without slots. (b) Model diagram of the 3D subunit with slots.

amplitude and phase shift [27]. Therefore, the 3D subunit structure with the slot still can be equivalent to the corresponding 2D one.

APPENDIX C: GEOMETRY OF FABRICATED DEM AND TEST SETUP

To accurately fabricate the metasurface, the computer numerical control (CNC) milling machine with a manufacturing precision of 0.01 mm is adopted. The DEMs in the experimental measurements are composed of identical processed resonators. For the processed plate, slots should be cut to separate adjacent different 3D subunits in a metasurface, as shown in Figs. 6–8. The adjacent slots make up many striplike models. Different numbers of processed resonators are attached to the striplike model to make up different subunits, which consist of the metasurface. The numbers in yellow fonts represent the different numbers of attached resonators in the striplike model, as shown in Figs. 6–8. These resonators can be conveniently disassembled and reattached because the glue layer is very thin; in addition, there is no need for the ordered arrangement of these resonators. This process enables the design of a disordered metasurface to achieve tunable multifunction by using one type of pillared resonator and the same hosting plate. For example, the fabricated metasurface in Fig. 6 can achieve anomalous deflection [the experimental results are shown in Figs. 3(e)], those in Figs. 7 and 8 can achieve negative deflection [the experimental results are shown in Figs. 3(f)] and focusing [the experimental results are shown in Fig. 4(d)], respectively.

An array of PZT-5A patches ($20 \times 20 \times 0.3$ mm^3) are bonded onto the surface of the plate as actuators. The spacing of adjacent piezoelectric patches is the same as the piezoelectric patch width, according to the phased array theory [12]. The widths of the DEMs only need to be larger than the width of the excited flexural beams. For simplicity, in the deflection experiments shown in Figs. 6 and 7, we adopt six piezoelectric patches (the total width is 220 mm) to excite flexural waves and 16 subunits to build the DEMs (the total width is 342.4 m). In the focusing experiments shown in Fig. 8, we adopt 12 piezoelectric patches (the total width is 460 mm) to excite flexural waves and 24 subunits to build the DEM (the total width is 513.6 mm). Under the control of the waveform editor (based on Labview software), a five-cycle tone burst is generated by the signal generator (Agilent 33220A) and then amplified by a power amplifier (HVPA05). The wave fields in the incident and transmitted areas are measured by the measurement mode "time" of the PSV-400 scanning laser Doppler vibrometer [27].

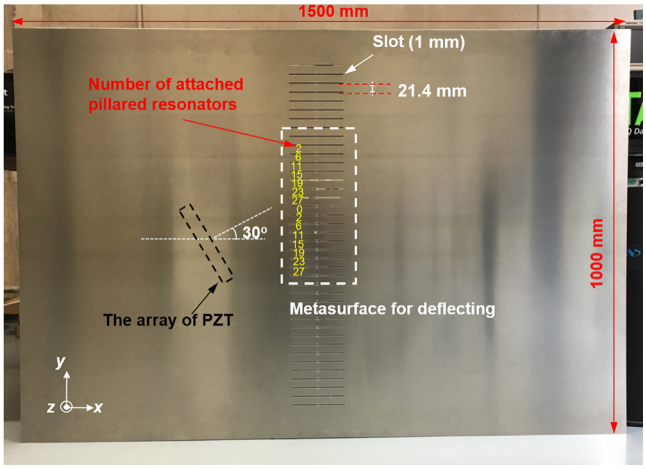

FIG. 7. Model diagram of the fabricated DEM with a phase shift gradient of $d\phi/dy = k$.

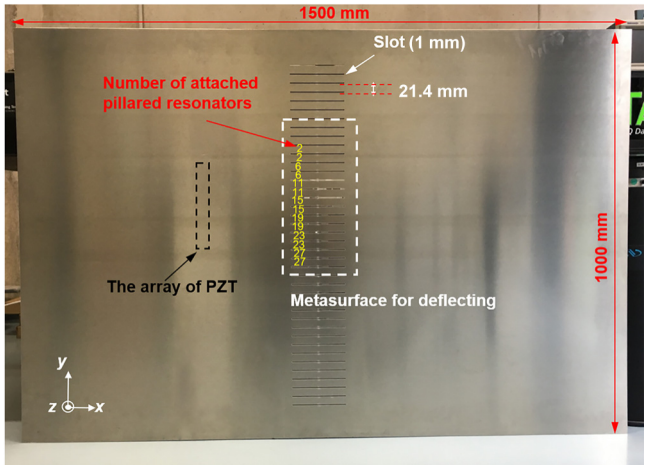

FIG. 6. Model diagram of the fabricated DEM with a phase shift gradient of $d\phi/dy = 0.5k$. PZT, piezoelectric transducer.

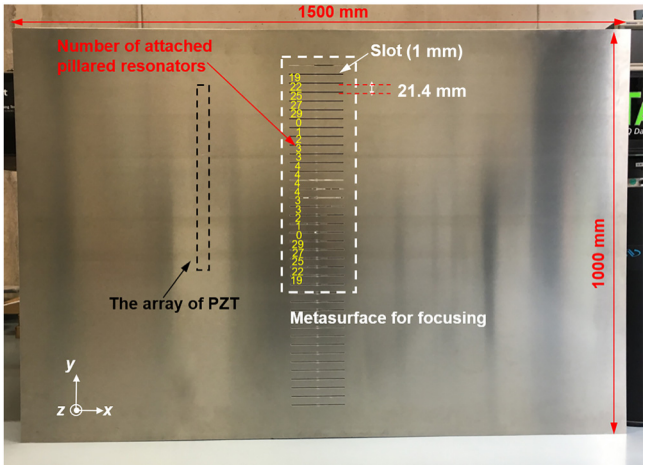

FIG. 8. Model diagram of the DEM with the desired focal distance of $F = 1.5\lambda$.

APPENDIX D: THE DESIGN OF THE RECONFIGURABLE SUBUNIT

The schematic diagram of the reconfigurable subunit is shown in Fig. 9. It can be seen from Fig. 9 that the reconfigurable subunit has some improvements compared with the disordered subunit in Fig. 1(b). A thin layer of iron (about 0.1 mm) is plated on the upper surface of the pillar by using a PVD system and magnetized as the N pole by annealing at 300 °C for 2.0 h in a magnetic field of 1 T [28]. Three electromagnets are placed above the pillars. The electromagnets have magnetic poles that can convert N and S into each other on the upper and lower surfaces. A plastic guide rod is attached to the upper surface of the pillar, which can flexibly move the position of the pillar.

The working principle is very simple. Magnetic fields in different directions are formed under the three energized electromagnets. For example, magnetic fields are N, N, and S poles for lower surfaces of electromagnets 1, 2, and 3, respectively. We can move the pillar through the plastic guide rod to select the application of repulsion or attraction by the magnetic field. Under electromagnets 1 and 2, the pillar is repulsed and attached to the host plate. Under electromagnet 3, the pillar is separated from the host plate due to magnetic attraction. Therefore, the number of pillars attached on the host plate can be reconstructed by moving the pillars to different magnetic fields. In this way, disorder has great advantages over order. The reason is that disorder releases the degree of freedom of the pillar position, which greatly enhances reconfigurability.

We also conduct a feasibility analysis for the designed structure. First, in the experiment, we can apply a small amount of oil on the lower surface of the pillar to fill the gap between the pillar and the host plate. This super-subwavelength oil layer not only ensures a good connection between the pillar and the host plate, but also ensures that it does not affect the propagation of waves at the joint interface. Then, the impedance of plastic and the thin iron layer is greatly mismatched, which will ensure that the lightweight plastic guide rod will not affect wave propagation in the pillar. Finally, applying a repulsive force to the pillar is equivalent to giving the pillar an axial prestress T. The differential element of the pillar is taken for analysis, as shown in Fig. 10. The equation of motion in the x direction, following Newton's second law ($\Sigma F = ma$), is as follows:

$$d_2\rho dz\frac{\partial^2 w}{\partial t^2} = V + \frac{\partial V}{\partial z}dz - V + T\varphi - T\left(\varphi + \frac{\partial \varphi}{\partial z}dz\right), \tag{D1}$$

where w is the displacement of the particle of the pillar in the x direction. Substituting the relationships $\varphi = \partial w/\partial z$ and $V = EI\frac{\partial^3 w}{\partial z^3}$ into Eq. (D1), we obtain

$$EI\frac{\partial^4 w}{\partial z^4} - T\frac{\partial^2 w}{\partial z^2} - \omega^2\rho d_2 = 0. \tag{D2}$$

From Eq. (D2), the flexural wave number can be obtained,

$$k_b^* = \pm\sqrt{\frac{T}{2EI} \pm \sqrt{\left(\frac{T}{2EI}\right)^2 + \frac{\omega^2\rho d_2}{EI}}}, \tag{D3}$$

where, $2EI = 353.5$. When $T/(2EI) < 0.06 \ll 1$, we can get $k_b^* \approx k_{b2}$. This indicates that the prepressure $[T/(2EI) < 0.06]$ does not affect the propagation of flexural waves in the pillar. Through the same analysis, we find that the prestress $[T/(2EI) < 0.06]$ barely affects the propagation of the longitudinal wave in the pillar and propagations of the flexural wave and the longitudinal wave in the plate. Therefore, prestress $[T/(2EI) < 0.06]$ does not affect the propagation of flexural waves and the longitudinal wave; at the same time, it can make the pillar stably attach to the host plate.

It should be noted that, for the x-direction boundary condition at the junction of the pillar and the host plate, the nonglued pillar in the above reconfigurable subunit may weaken it compared with the glued pillar. We can reduce the height of the pillared resonator or decrease the rigidity of the pillared resonator, so that the vibration of the pillared

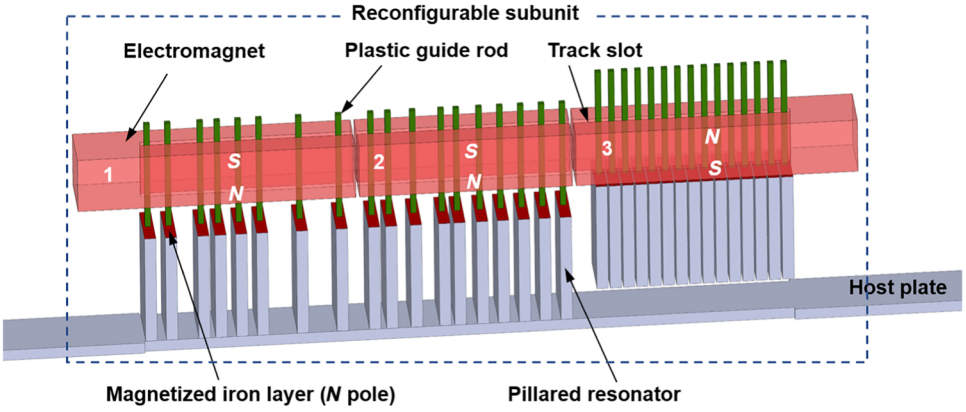

FIG. 9. Schematic diagram of the reconfigurable subunit.

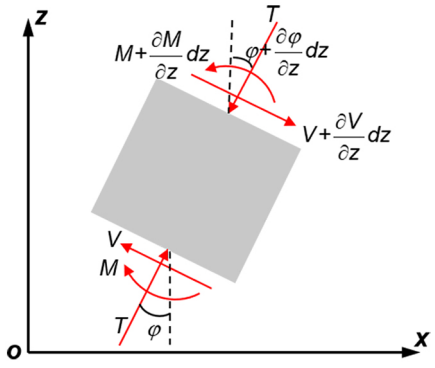

FIG. 10. Differential element of the pillar resonator.

resonator can couple into the host plate, with the dominant effect coming from the compressional modes of the resonator [10,29]; in other word, the y-direction boundary condition will be dominant at the junction of the resonator and the host plate. In this way, it can eliminate the impact of weakened x-direction boundary conditions.

APPENDIX E: METHOD FOR NUMERICAL SIMULATIONS

All pillared resonators and the plate are made of aluminum alloy, with an elastic modulus of $E_{\mathrm{Al}} = 70\,\mathrm{GPa}$, a Poisson's ratio of $\nu_{\mathrm{Al}} = 0.33$, and density of $\rho_{\mathrm{Al}} = 2700\,\mathrm{kg/m^3}$. The phase shift and transmission amplitude for the 2D subunits are obtained using COMSOL Multiphysics 5.4 software (plane strain module). Perfectly matched layers (PMLs) are used on both ends of every striplike model to avoid any reflection from the boundaries. An exciting force is applied normally on the surface of the left part of the plate [at point P in Fig. 1(c)]. The phase shift and transmission amplitude of the excited flexural wave in the far field of the right part of the plate (at point Q) are examined by varying the number of resonators j in the subunit. All full-wave simulations for the metasurface are obtained using COMSOL Multiphysics 5.4 software (solid mechanics module). For all simulations on the wave patterns of metasurfaces, PMLs are used on all outer boundaries.

APPENDIX F: SIMULATIONS AND MEASUREMENTS FOR THE ORDERED METASURFACES

The ordered elastic metasurface with a uniform pillar spacing of 5 mm is also constructed to achieve anomalous deflection and negative deflection. The full-field experimental measurement is shown in Figs. 11(c) and 11(d).

The ordered elastic metasurface with a uniform pillars spacing of 5 mm is constructed to achieve flexural wave focusing. The full-field experimental measurement is shown in Fig. 12(d).

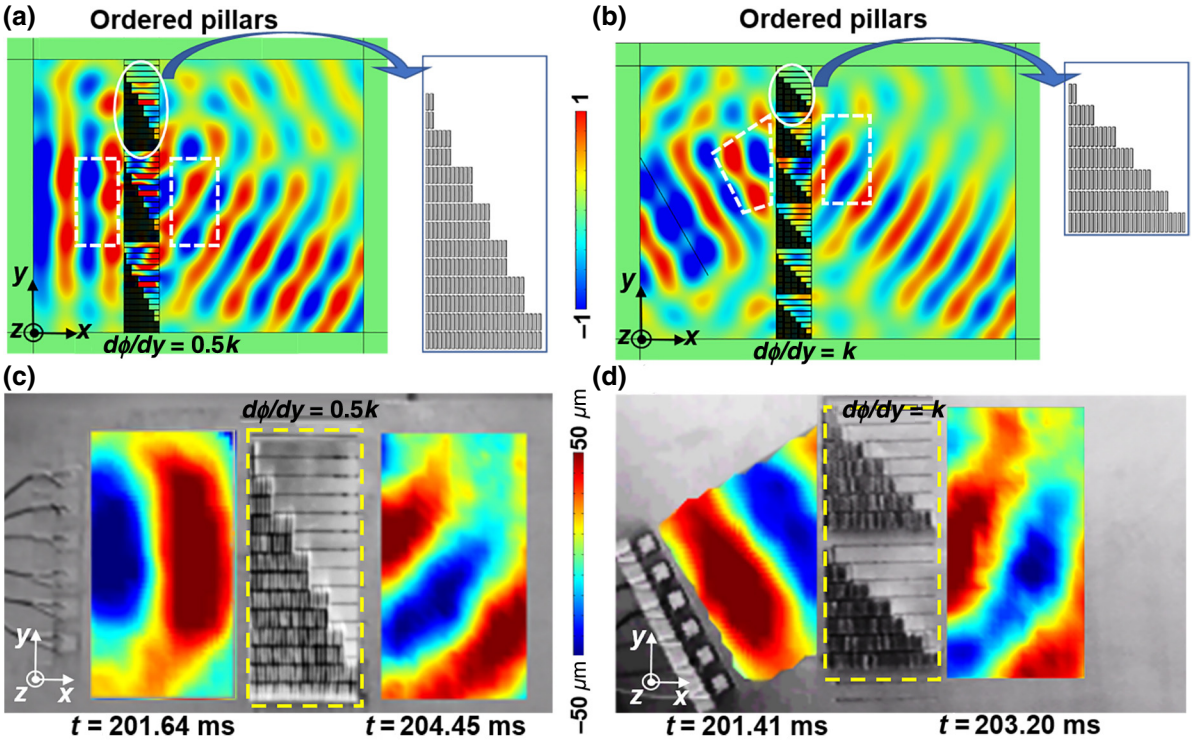

FIG. 11. (a),(b) Wave fields for vertical and oblique incident flexural wave Gaussian beams passing through two ordered metasurfaces, with phase-shift gradients of $d\phi/dy = 0.5k$ and $d\phi/dy = k$, respectively. (c),(d) Full-field experimental measurements.

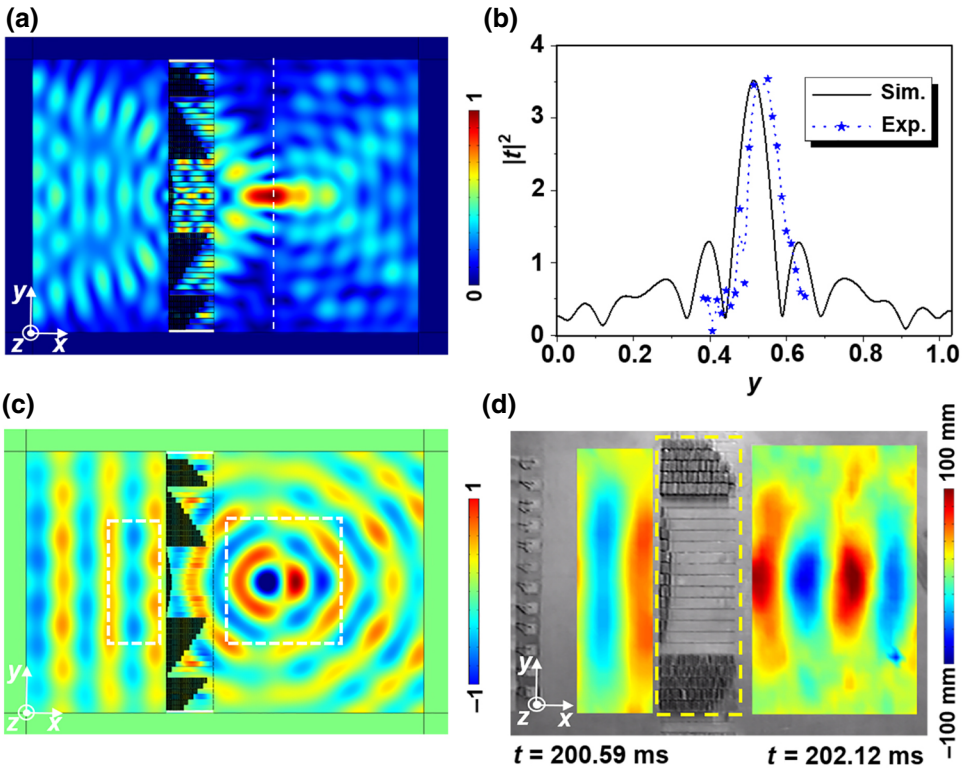

FIG. 12. (a),(c) Numerical transmitted intensity and displacement fields with focus at 1.5λ for the ordered elastic metasurface, respectively. (b) Normalized simulated and experimental transmitted intensity at the focal spot along the y direction ($x = 1.5\lambda$). (d) Experimental measurement.

[1] F. Baboux, L. Ge, T. Jacqmin, M. Biondi, E. Galopin, A. Lemaître, L. L. Gratiet, I. Sagnes, S. Schmidt, H. E. Türeci, A. Amo, and J. Bloch, Bosonic Condensation and Disorder-Induced Localization in a Flat Band, Phys. Rev. Lett. **116**, 066402 (2016).

[2] G. M. Conley, M. Burresi, F. Pratesi, K. Vynck, and D. S. Wiersma, Light Transport and Localization in Two-Dimensional Correlated Disorder, Phys. Rev. Lett. **112**, 143901 (2014).

[3] D. Nau, A. Schonhardt, C. Bauer, A. Christ, T. Zentgraf, J. Kuhl, M. W. Klein, and H. Giessen, Correlation Effects in Disordered Metallic Photonic Crystal Slabs, Phys. Rev. Lett. **98**, 133902 (2007).

[4] S. Hughes, L. Ramunno, J. F. Young, and J. E. Sipe, Extrinsic Optical Scattering Loss in Photonic CrystalWaveguides: Role of Fabrication Disorder and Photon Group Velocity, Phys. Rev. Lett. **94**, 033903 (2005).

[5] P. Celli, B. Yousefzadeh, C. Daraio, and S. Gonella, Bandgap widening by disorder in rainbow metamaterials, Appl. Phys. Lett. **114**, 091903 (2019).

[6] A. A. Asatryan, L. C. Botten, M. A. Byrne, V. D. Freilikher, S. A. Gredeskul, I. V. Shadrivov, R. C. McPhedran, and Y. S. Kivchar, Suppression of Anderson Localization in Disordered Meta-materials, Phys. Rev. Lett. **99**, 193902 (2007).

[7] V. Bellani, E. Diez, R. Hey, L. Toni, L. Tarricone, G. B. Parravicini, F. Domínguez-Adame, and R. Gómez-Alcalá, Experimental Evidence of Delocalized States in Random Dimer Superlattices, Phys. Rev. Lett. **82**, 2159 (1999).

[8] C. Liu, W. Gao, B. Yang, and S. Zhang, Disorder-Induced Topological State Transition in Photonic Metamaterials, Phys. Rev. Lett. **119**, 183901 (2017).

[9] A. Rahimzadegan, D. Arslan, R. N. S. Suryadharma, S. Fasold, M. Falkner, T. Pertsch, I. Staude, and C. Rockstuhl, Disorder-Induced Phase Transitions in the Transmission of Dielectric Metasurfaces, Phys. Rev. Lett. **122**, 015702 (2019).

[10] M. Rupin, F. Lemoult, G. Lerosey, and P. Roux, Experimental Demonstration of Ordered and Disordered Multiresonant Metamaterials for Lamb Waves, Phys. Rev. Lett. **112**, 234301 (2014).

[11] P. B. Catrysse and S. Fan, Routing of deep-subwavelength optical beams and images without reflection and diffraction using infinitely anisotropic metamaterials, Adv. Mater. **25**, 194 (2013).

[12] R. Zhu, X. N. Liu, G. K. Hu, C. T. Sun, and G. L. Huang, Negative refraction of elastic waves at the deep-subwavelength scale in a single-phase metamaterial, Nat. Commun. **5**, 5510 (2014).

[13] J. M. Kweun, H. J. Lee, J. H. Oh, H. M. Seung, and Y. Y. Kim, Transmodal fabry-perot resonance: Theory and realization with elastic metamaterials, Phys. Rev. Lett. **118**, 205901 (2017).

[14] N. F. Yu, P. Genevet, M. A. Kats, F. Aieta, J. P. Tetienne, F. Capasso, and Z. Gaburro, Light propagation with phase discontinuities: Generalized laws of reflection and refraction, Science **334**, 333 (2011).

[15] E. Bok, J. J. Park, H. Choi, C. K. Han, O. B. Wright, and S. H. Lee, Metasurface for Water-to-Air Sound Transmission, Phys. Rev. Lett. **120**, 044302 (2018).

[16] B. Assouar, B. Liang, Y. Wu, Y. Li, J. Cheng, and Y. Jing, Acoustic metasurfaces, Nat. Rev. Mater. **3**, 460 (2018).
[17] Y. Li, C. Shen, Y. Xie, J. Li, W. Wang, S. A. Cummer, and Y. Jing, Tunable asymmetric transmission via Lossy acoustic metasurfaces, Phys. Rev. Lett. **119**, 035501 (2017).
[18] Y. Zhu, J. Hu, X. Fan, J. Yang, B. Liang, X. Zhu, and J. Cheng, Fine manipulation of sound via lossy metamaterials with independent and arbitrary reflection amplitude and phase, Nat. Commun. **9**, 1632 (2018).
[19] S. W. Fan, S. D. Zhao, A. L. Chen, Y. F. Wang, B. Assouar, and Y. S. Wang, Tunable Broadband Reflective Acoustic Metasurface, Phys. Rev. Appl. **11**, 044038 (2019).
[20] H. Zhu and F. Semperlotti, Anomalous refraction of acoustic guided waves in solids with geometrically tapered metasurfaces, Phys. Rev. Lett **117**, 034302 (2016).
[21] Y. Q. Liu, Z. X. Liang, F. Liu, O. Diba, A. Lamb, and J. S. Li, Source illusion devices for flexural lamb waves using elastic metasurfaces, Phys. Rev. Lett **119**, 034301 (2017).
[22] M. Jang, Y. Horie, S. M. Kamali, A. Shibukawa, A. Arbabi, J. Brake, H. Ruan, Y. Liu, A. Faraon, and C. Yang, Wavefront shaping with disorder-engineered metasurfaces, Nat. Photonics **12**, 84 (2018).
[23] Y. L. Xu, L. Y. Cao, and Z. C. Yang, Deflecting incident flexural waves by nonresonant single-phase meta-slab with subunits of graded thicknesses, J. Sound. Vib **454**, 51 (2019).
[24] J. Zhang, X. Su, Y. L. Liu, Y. X. Zhao, X. Jing, and N. Hu, Metasurface constituted by thin composite beams to steer flexural waves in thin plates, Int. J. Solids Struct **162**, 14 (2018).
[25] See the Supplemental Material at http://link.aps.org/supplemental/10.1103/PhysRevApplied.13.014054 for detailed propagation phenomena for the anomalous deflections and focusing.
[26] Y. B. Jin, E. El Boudouti, Y. Pennec, and B. Djafari-Rouhani, Tunable fano resonances of lamb modes in a pillared metasurface, J. Phys. D. Appl. Phys **50**, 425304 (2017).
[27] L. Y. Cao, Z. C. Yang, Y. L. Xu, and B. M. Assouar, Deflecting flexural wave with high transmission by using pillared elastic metasurface, Smart Mater. Struct **27**, 075051 (2018).
[28] Z. M. Zeng, P. Upadhyaya, P. K. Amiri, K. H. Cheung, J. A. Katine, J. Langer, K. L. Wang, and H. W. Jiang, Enhancement of microwave emission in magnetic tunnel junction oscillators through in-plane field orientation, Appl. Phys. Lett **99**, 032503 (2011).
[29] D. J. Colquitt, A. Colombi, R. V. Craster, P. Roux, and S. R. L. Guenneau, Seismic metasurfaces: Sub-wavelength resonators and Rayleigh wave interaction, J. Mech. Phys. Solids, **99**, 379 (2017).